Pergamon

Int. J. Solids Structures Vol. 35, No. 12, pp. 1137–1161, 1998

0020 7683/98 $19.00 + .00

PII: S0020-7683(97)00096-6

IDENTIFYING FAILURE MECHANISMS OF COMPOSITE STRUCTURES UNDER COMPRESSIVE LOAD

L. C. WU, C. Y. LO, T. NAKAMURA†, A. KUSHNER
Department of Mechanical Engineering, State University of New York at Stony Brook, Stony Brook, NY 11794-2300, U.S.A.

(*Received* 1 *March* 1996; *in revised form* 24 *March* 1997)

Abstract—Various failure mechanisms involving both local and global deformation mechanisms of layered structures, consisting of differently oriented orthotropic laminae, are investigated with a large deformation finite element analysis. Under large compressive loads, fiber-reinforced composite structures can fail by buckling, kink band formation and/or delamination growth. Our aim is to identify the dominant mode which leads to the structural failure under a given boundary condition and geometrical shape. It is assumed that these structures contain initial interlaminar flaws represented by embedded delaminations. Such flaws can play a significant role in defining overall structural integrity and deformation mechanisms. Our study considers two structures with distinguished shapes, both consisting of four layer laminae. The first structure is a flat panel under compressive load and the second structure is a cylindrical shell subjected to external pressure. In both cases, the energy release rate and mixed-mode stress intensity factors are computed to quantify the crack driving force and used to measure likelihood of delamination growth. In the flat panel model, two buckling modes, a global and a local, are observed under quasi-static loading conditions. Depending upon the delamination length and laminate stacking orientations, the interaction of these two modes can produce an unstable post-buckling behavior. It is found that the energy release rate exceeds experimentally estimated fracture toughness values only after buckling occurs. In the cylindrical shell study, lower critical buckling loads are observed for models with longer interlaminar delamination as in the flat panel model. However, unlike the flat panel case, the energy release rate surpasses the critical toughness well before the applied pressure reaches the buckling load of the flawed cylindrical shell. This behavior implies that a shell containing an embedded defect along an interface can fail by delamination growth and therefore has a failure load lower than its critical buckling load. Also, for thicker cylindrical shells, the compressive internal stress exceeds the predicted stress required for kink band formation prior to structural buckling. The competition among these failure modes, buckling, delamination growth and compressive kinking in fiber-reinforced composite structures, is studied and a design diagram is introduced here. This diagram predicts a likely dominant failure mode for given structural dimensions and material properties. In addition, unstable delamination growth along the lamina interface under dynamic loading conditions is simulated using an iterative computational procedure. The results predict that the crack tip velocity can reach a fraction of the material wave speed leading to total structural failure in a very short time. For the cylindrical shell, the inertial effect on the pressure-deformation relation is investigated by comparing it with the static results. © 1998 Elsevier Science Ltd.

1. INTRODUCTION

Due to their low weight and high strength, laminated composite materials are widely used in many applications for engineering structures. However, composite materials are subject to delaminations due to fabrication defects, imperfections, mismatch between different fiber orientations, or misalignment of fibers. When layered structures are subjected to compressive loads or impact forces, they can deform and fail in combinations of interacting modes, such as local and global buckling, kink band formation and broadening, or delamination growth. An earlier study (Nakamura *et al.*, 1995) showed that an embedded delamination can trigger collapse at a load level lower than the critical buckling load. In this investigation, we attempt to identify the dominant failure modes and determine under what conditions these failure modes occur.

Since delamination often occurs between two laminae with different fiber orientations, it is necessary to model the interface crack between two orthotropic materials. Recently Ting (1986) and Qu and Bassani (1989) have studied the static oscillatory fields near a

† Author to whom correspondence should be addressed.

crack tip and other characteristics of an interface crack in anisotropic materials. For a crack propagating dynamically under steady state conditions, Yang *et al.* (1991) derived the asymptotic crack tip field using the analytical method for anisotropic materials introduced by Stroh (1962). Stroh's formulation was also adopted in the various static problems solved by Suo (1990). For studying the transient dynamic problem, an effective computational method was proposed by Lo *et al.* (1994) and it was used to analyze dynamic crack propagation in composite laminae.

From the structural point of view, existence of embedded flaws can lower the critical buckling load and significantly alter the post-buckling behaviors of structures. The pre- and post-buckling behavior of composite laminates has been studied by Chai *et al.* (1981), Simitses *et al.* (1985), Wang (1985), Shivakumar and Whitcomb (1985), Kardomateas and Schmueser (1988), Yin (1988), Sheinman and Soffer (1991) and Nakamura *et al.* (1995). The behavior of delaminations under dynamic loadings was also investigated by Grady and Sun (1986), Sun and Manoharan (1988), and Wang *et al.* (1984). Useful experiments for analyzing buckling in structures with delaminations were developed by Jones *et al.* (1985) and Horban and Palazotto (1987).

An additional mode of compressive failure observed in fiber-reinforced composites is kink band initiation and growth. A model to predict the peak and steady state stresses in kink bands under compressive loading was recently presented by Liu and Shih (1995) and Fleck *et al.* (1995). Experimental results of kink band formation and its band broadening were also presented in Moran *et al.* (1995) and Jelf and Fleck (1992).

In this study, effective computational procedures based on fracture and structural mechanics approaches are used to characterize the behaviors of buckling and the interlaminar delamination between orthotropic materials. The analysis includes a parametric study of the influence of geometric and crack variables. Based on the computed results, we determine the effect of delamination on the overall structural strength and stability and identify the likely failure mechanism for given geometry and material parameters. We have also performed the analysis under dynamic loading conditions. The results are used to quantify the difference between the results of relevant parameters in the static and dynamic cases.

2. FAILURE MECHANISMS

2.1. *Structural buckling*

Thin structures under compressive load often fail by buckling. The stability problems of composite structures with delamination have been studied by several investigators. Many analytical solutions of buckling and post-buckling based on the Rayleigh–Ritz method, perturbation technique, the von Karman kinematic approach, and thin film models are derived by Wang *et al.* (1985), Kardomateas and Schmueser (1988), Sheinman and Soffer (1991) and Chai *et al.* (1981). In our previous study (Nakamura *et al.*, 1995), we found that composite plates subjected to compressive loading are influenced by two different buckling modes. One, which characterizes the overall panel buckling, is referred to as global buckling. The other, which is dominated by buckling of the delaminated ligament, is identified as local buckling. Coupling of the two nodes not only lowers the critical load for the flawed structure, but also may induce an *unstable* post-buckling behavior depending upon the delamination size. It should be noted that previous works cited did not explicitly model the crack tip deformation of the delamination, and did not show an unstable buckling behavior.

Due to the complex geometries and local details of many structures, finite element procedures are widely used for buckling analysis. The linearized buckling modes and critical loads can be evaluated by the eigenvalue extraction technique. For structures with stable post-buckling behavior such as beams, plates, and laterally loaded cylinders, the results of linear bifurcation buckling calculations generally give a realistic estimate of buckling strength. For imperfection sensitive structures with unstable initial post-buckling paths, the actual buckling strength can be significantly reduced from that predicted by the linearized analysis. Beginning with the work of Bijlaard and Fisher (1953), a growing appreciation of

the role of local buckling modes on reducing the buckling load of a structure has been established. Van der Neut (1969) proved that buckling mode interaction can lead to unstable branches for structures in which each individual buckling mode has a stable post-buckling path. Tvergaard (1976) analyzed the behavior of stiffened panels with nearly coincident local and global buckling loads. He found a very strong sensitivity of the initial post-buckling behavior for small imperfections but far less sensitivity to larger imperfections. This is quite similar to the behavior reported in our previous study (Nakamura *et al.*, 1995) for flat panels with initial delaminations. In this work, small initial delaminations lead to unstable buckling with a sharp drop in the load-displacement response. Initial delaminations beyond a critical size were found to lead to a reduced buckling load but a stable post-buckling behavior.

2.2. *Kink band failure*

For thicker structures with aligned fiber-reinforced composite laminae, kink bands are a common compressive failure mode. The key features controlling the kinking mechanism are initial fiber misalignment and interlaminar matrix shear strength. A kink band typically lies at an angle of 10 to 30 degrees relative to the normal direction of the fibers. The initial kink band width is typically about 10 fiber diameters. The initial kink band formation is caused by fiber bending and rotation and matrix deformation. These behaviors will gradually soften the band structure and initiate subsequent rapid fiber rotation, bending, and larger matrix shearing deformation. This stage will be arrested by fiber lock up at a fiber rotation of about 40 to 45 degrees. The kink band will begin to broaden within the band at this orientation until fiber breaking occurs. Such phenomena are discussed in detail in the various papers dealing with the kink band formation. The governing equation for kink band initiation in plane stress with remote applied pressure can be expressed by $(\sigma_1-\sigma_2)\eta+\tau=\tau_c$, where σ_1 and σ_2 are the remote normal stresses, τ is the remote shear stress, η characterizes the fiber misalignment and the elastic deformation at incipient kinking, and τ_c is the critical resolved shear yield strength of the matrix. For steady-state conditions, Moran *et al.* (1995) have formulated an expression for the steady state kink band stress σ_{KB} using a piece-wise linear approximation model

$$\sigma_{KB}=\frac{1}{2\sin^2\beta}\left[\tau_y\left(2\tan\beta-\frac{\gamma_y}{2}\right)+\frac{1}{2}G_s(2\tan\beta-\gamma_s)^2\right], \tag{1}$$

where β is kink band orientation, τ_y and γ_y are the yield shear stress and strain, G_s and γ_s are the secondary (hardening) modulus and its critical strain, respectively. The minimum σ_{KB} in (1) corresponds to the steady state kink band stress. Using the models given by Liu and Shih (1995) and the experimental analysis of Jelf and Fleck (1992), epoxy reinforced with carbon fibers shows $\sigma_c \sim 1.3$ GPa and 132 MPa $< \sigma_{KB} <$ 330 MPa when the values $\beta = 22^\circ$, $\tau_c = 80$ MPa and $\eta = 0.06$ are chosen.

2.3. *Delamination growth*

Interfacial delamination is another possible mode of compressive failure, perhaps unique to composite laminates. Initial flaws within the structures may be due to weak bonding of laminae, fiber misalignment, and voids and defects developed during the manufacturing process. Such embedded flaws are often observed at the interface of two laminae with different orientations of fibers. These interlaminar flaws or delaminations essentially remain closed during low compressive load. Once significant geometry change occurs, the driving force for the delamination growth, the energy release rate increases rapidly. This is especially so near the buckling load or during the unstable post-buckling phase. When the critical toughness is reached, the delamination will grow and cause the entire structure to fail.

In order to characterize the driving force for delamination growth quantitatively, the energy release rate must be calculated accurately. Using the domain integral formulation, the energy release rate of a crack tip propagating along the x_1 direction is given as,

$$\mathcal{G} = \int_A \left[\sigma_{ij} \frac{\partial u_i}{\partial x_1} \frac{\partial q}{\partial x_j} - (W+T)\frac{\partial q}{\partial x_1} + \rho\left(\frac{\partial^2 u_i \partial u_i}{\partial t^2 \partial x_1} - \frac{\partial u_i}{\partial t}\frac{\partial^2 u_i}{\partial x_1 \partial t} \right) q \right] \mathrm{d}A, \tag{2}$$

where A is the domain enclosed by arbitrary path which surrounds the crack tip and the weighting parameter q is a smooth function of x_1 and x_2. Also, σ_{ij} and u_i are the Cartesian components of stresses and displacements, respectively, W is the strain energy density and T is the kinetic energy density at a material point. Under static loading condition, the terms associated with time derivatives in (2) vanish.

The relationship between the energy release rate and the stress intensity factors for a dynamically propagating interface crack was shown by Yang *et al.* (1991) as

$$\mathcal{G} = \frac{H_{22}}{4\cosh^2(\pi\varepsilon)} |\mathbf{K}|^2, \tag{3}$$

where $\mathbf{K}$ is the complex stress intensity factor and is given by $\mathbf{K} = K_1 + iK_{II}$. Also, H_{22} is a component of the hermitian matrix $\mathbf{H}$ and ε is the oscillatory index. Both $\mathbf{H}$ and ε depend on material properties as well as the crack tip speed in the dynamic case. The complete expressions are very complex and they are shown in Nakamura *et al.* (1995). Note that H_{22} has a complex form for orthotropic bimaterials but reduces to $4/E^*$ for a stationary crack in isotropic bimaterials, where E^* is the effective tensile modulus. The phase angle ψ is another important parameter in defining the fracture toughness or the critical energy release rate of an interface crack. Many experimental studies have shown that the critical energy release rate can be defined as a function of the phase angle, i.e., $\mathcal{G}_c(\psi)$. It is essentially the ratio of the shear to normal traction ahead of the crack tip. The phase angle varies with the distance from the tip due to the oscillatory nature of the field. Thus, the phase angle must be defined in terms of a characteristic length scale L as

$$\psi(L) = \tan^{-1}\left\{ \frac{\mathrm{Im}[\mathbf{K}L^{i\varepsilon}]}{\mathrm{Re}[\mathbf{K}L^{i\varepsilon}]} \right\}. \tag{4}$$

In our analysis, we have chosen $L = 100\ \mu$m, which has been used in reporting the results of many bimaterial experiments. In order to determine the phase angle, it is necessary to calculate each mode of the stress intensity factor. The most accurate method to extract mixed-mode stress intensity factors in elastic solids has been shown to be the "interaction integrals" method (Lo *et al.*, 1994). This integral in domain integral form is

$$I = \int_A \left[\left(\sigma_{ij} \frac{\partial u_i^{\mathrm{aux}}}{\partial x_1} + \sigma_{ij}^{\mathrm{aux}} \frac{\partial u_i}{\partial x_1} \right) \frac{\partial q}{\partial x_j} - \left(\sigma_{ij}\varepsilon_{ij}^{\mathrm{aux}} + \rho \frac{\partial u_i}{\partial t}\frac{\partial u_i^{\mathrm{aux}}}{\partial t} \right) \frac{\partial q}{\partial x_1} \right.$$
$$\left. + \rho\left(\frac{\partial^2 u_i}{\partial t^2}\frac{\partial u_i^{\mathrm{aux}}}{\partial x_1} + \frac{\partial^2 u_i^{\mathrm{aux}}}{\partial t^2}\frac{\partial u_i}{\partial x_1} - \frac{\partial^2 u_i}{\partial x_1 \partial t}\frac{\partial u_i^{\mathrm{aux}}}{\partial t} - \frac{\partial u_i}{\partial t}\frac{\partial^2 u_i^{\mathrm{aux}}}{\partial x_1 \partial t} \right) q \right] \mathrm{d}A. \tag{5}$$

Here the terms with the superscript "aux" are the auxiliary functions defined from a known solution. Using the dynamic interaction integral (5) and the relation between the energy release rate and dynamic stress intensity factor (3), one can effectively extract the mode I and II stress intensity factors from the computed solution. The following equation gives the relationship between the dynamic interaction integral I and the stress intensity factors of the actual and auxiliary fields,

$$I = \frac{H_{22}}{2\cosh^2(\pi\varepsilon)} (K_I K_I^{\mathrm{aux}} + K_{II} K_{II}^{\mathrm{aux}}). \tag{6}$$

This is the fundamental equation which connects the computable interaction integral I

shown in (5) to the unknown stress intensity factors of the dynamic interface crack **K**. A more detailed description of the procedure for extraction of those stress intensity factors is given by Lo *et al.* (1994).

Since the models are loaded into the post-buckling regime, a large deformation finite element analysis is employed. Throughout the calculations, strains are expected to remain relatively small while rotations can be large. In order to account for the large rotations, the energy release rate and the stress intensity factors are computed by the following procedure. First the current direction of crack tip is determined from the upper and lower crack planes near the tip and it is taken as the local x_1 direction. Then the displacement vectors at every node within the largest integration domain A are rotated to the local coordinate system by a coordinate transformation. All the other field quantities in (2) and (5) are recalculated in terms of the transformed displacement field at every load increment. This could be interpreted as a corotational formulation of the crack tip analysis.

If the criterion for crack growth is controlled by the energy release rate, delamination or crack growth occurs when the driving force $\mathcal{G}$ is equal to the critical energy release rate $\mathcal{G}_c$. Naturally, we postulate that $\mathcal{G}_c$ be a function of the phase angle in composite solids as in the case of isotropic bimaterial. However due to a lack of sufficient experimental data, we assume the criterion for crack growth initiation to be independent of the phase angle in the current analysis. Grady and Sun (1986) and Wang *et al.* (1984) have reported the measured toughness $\mathcal{G}_c$ for graphite reinforced epoxy laminate to range from 0.3 kJ/m^2 to 1 kJ/m^2. In the section where a failure mode diagram is presented, the initiation toughness is chosen as $\mathcal{G}_c = 0.72$ kJ/m^2. For the dynamic part of analysis discussed in Section 5, we further assume, for simplicity of interpreting computed results, that the dynamic initiation toughness $\mathcal{G}_d$ as well as the dynamic crack propagation toughness $\mathcal{G}_D$ is constant and identical to the static value, i.e., $\mathcal{G}_c = \mathcal{G}_d = \mathcal{G}_D = 0.72$ kJ/m^2. In Lo *et al.* (1994) and Nakamura *et al.* (1995), several forms of $\mathcal{G}_D$ which depend on the phase angle and the crack tip velocity were proposed for isotropic bimaterial interface cracks. A similar expression for the interface crack between differently oriented laminae is possible, but it would require extensive experimental investigations. We note, however, that any dynamic toughness criteria can be easily accommodated in the simulation procedure developed here.

3. COMPOSITE STRUCTURES WITH EMBEDDED DELAMINATION

3.1. *Flat panel model*

To determine the effect of an embedded delamination on the overall deformation mode in composite structures, we initially consider a thin flat composite panel consisting of four differently oriented orthotropic laminae. This model was also considered in our previous analysis (Nakamura *et al.*, 1995). However, in the current analysis, the applications of the initial geometric perturbation and loading boundary condition are refined and more accurate results are obtained. The panel is subjected to horizontal compressive load applied at the ends as shown in Fig. 1(a). The length of this panel is chosen to be $2L = 1$ m and the total width of the four bonded laminae is set at $t = 0.02$ m. Plane strain conditions and unit thickness in the out-of-plane direction are assumed. At the center of the panel, we model a finite interlaminar delamination of length $2a$ between the first and second layers from the bottom. Each layer has identical material properties which are modeled to represent a typical epoxy reinforced by unidirectional graphite fibers. The transversely isotropic model is used to represent the material behavior and the material constants are chosen as $E_L = 103$ GPa, $E_T = 6$ GPa, $G_{TT} = 2.1$ GPa, $G_{LT} = 5.3$ GPa, $\nu_{LT} = 0.3$ and $\rho = 138$ kg/m^3, where the fiber direction is denoted by subscript "L" and the transverse direction is denoted by "T". The transverse direction is defined as the plane of isotropy. In 2D finite element analysis, only two fiber orientations are compatible with plane strain condition and they are 0° and 90°, where 0° indicates the fiber direction parallel to the panel while the fiber direction of 90° is the out-of-plane direction. The 0° orientation is much stiffer than the 90° orientation with respect to the in-plane horizontal force. There are two possible laminate stacking sequences which are symmetrical about the mid-horizontal line. They are [0°/90°/90°/0°] and [90°/0°/0°/90°] combinations. Since the latter arrangement yields very

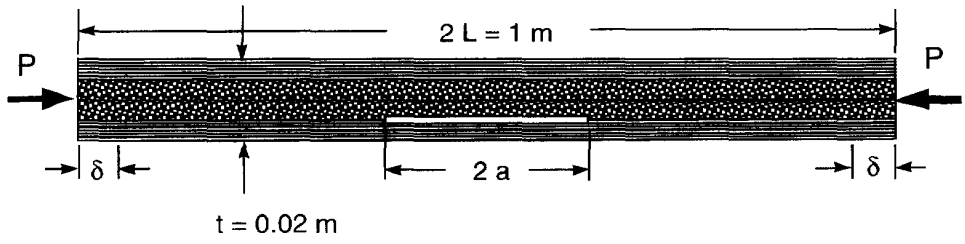

(a)

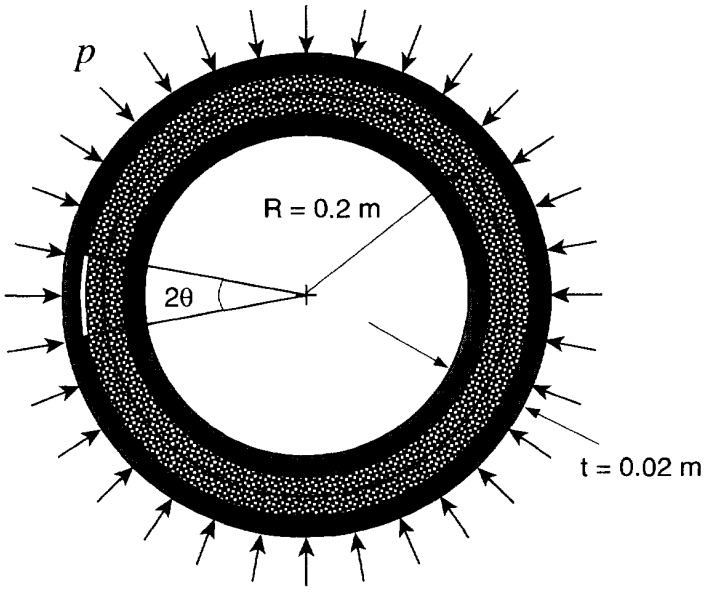

(b)

Fig. 1. Schematic of two composite structures consisting of four orthotropic laminae. The orientations of laminae are [0/90°/90°/0°]. (a) Flat panel which contains an interlaminar delamination between the third and fourth layers from the top and subjected to compressive axial load. (b) Cylindrical shell which contains a delamination between the first and second layers from the outer surface and subjected to external pressure.

weak resistance against flexure, only the former case is considered in this analysis. Effects of different stacking sequences including the latter case and panels with greater number of laminae are investigated in Wu and Nakamura (1997). In carrying out the finite element analysis, several computational models are constructed for different delamination lengths. Since this model possesses a symmetrical condition across the mid-section, only the right-half of the panel is modeled in the finite element analysis. The symmetry boundary condition is prescribed in the horizontal direction along the vertical mid-plane. Due to the possibility of unstable deformation, the compressive load application is controlled by increasing the end-shortening displacement δ. Furthermore, the displacements of the entire nodes along the end plane are constrained in such a way that large local deformation in the middle node is avoided. The total reaction forces at these nodes are reported as the equivalent applied load P. The finite element meshes for various delamination lengths are generated by a mesh generator program which accurately models the crack tip region and the transition to a coarser mesh. Each mesh contains about 6500 4-noded plane strain elements for the half-model. As in other fracture analyses, sufficiently small elements are employed near the delamination tip (the smallest near tip element size is about $0.01t$). However the elements throughout the model are also kept small enough (the largest element length is less than

$0.1t$) so that the buckling modes can be captured accurately. To estimate the accuracy of the reported results, we compared solutions from a model using quadruple the number of elements and found the solutions to be nearly the same. During the loading range of interest, we find that strains remain relatively small ($|\varepsilon_{max}| < 0.03$ at $\mathcal{G} = 1$ kJ/m^2) but the rotation becomes quite large.

3.2. *Cylindrical shell model*

In order to study the effect of structural geometry under compressive loading, we have chosen a cylindrical shell subjected to an external pressure as the next model. This choice is made not only because it is perhaps the second most common geometry next to a flat panel but also it has deformation characteristics quite distinct from the flat panel case. First, it is known that the post-buckling deformation of a long cylinder under external pressure exhibits more *stable* behavior than that of the flat panel. Second, the magnitude of internal hoop stress at the buckling load is significantly higher in the pressurized cylindrical geometries considered here. As in the flat panel, the cylindrical shell is also made of four differently oriented orthotropic laminae with the stacking sequence [0°/90°/90°/0°] as shown in Fig. 1(b). Here 0° indicates fibers in the circumferential direction while the 90° corresponds to a lamina whose fibers are in the out-of-plane or the axial direction of the cylinder. In this model, the shell radius is chosen to be $R = 0.2$ m and the thickness is set at $t = 0.02$ m. As in the case of flat panel model, we assume an interlaminar delamination to exist between the first and second layers from the outside. To conform to the arc of the cylinder, the delamination is curved and its size or arc length is measured by the so-called delamination angle, 2θ. For each laminate, the identical material properties as the flat panel are assumed. But, unlike the flat panel case, the loading can not be controlled through the equivalent displacement in the cylindrical model due to its geometrical condition, and the actual radial pressure must be applied uniformly over the outer element boundary of the shell. Although such a loading condition is more difficult to impose in any buckling analysis, this problem is overcome by taking extremely small load increments near the buckling regime. Fast convergence techniques such as the RIKS method are not suitable here since the near tip field is found to be sensitive to the size of load increment. We also note that any force controlled boundary condition can never be used in the flat panel analysis since some models exhibit highly unstable post-buckling behavior, but a more stable load-deflection relation in the cylindrical case makes such a loading condition possible. In constructing the finite element mesh, we consider only the top half of the cylindrical shell since it possesses a symmetry across the mid-horizontal plane. The symmetry condition is imposed by fixing the vertical displacements of the nodes along the horizontal section. A mesh generator program is again used to construct meshes with different delamination lengths. A typical mesh with 8540 4-noded plane strain elements is shown in Fig. 2. As in the case of the flat panel, accurate simulation of buckling deformation requires every element in the model to be relatively small. The near tip region of the mesh is enlarged and also depicted in Fig. 2.

4. COMPUTATIONAL RESULTS

4.1. *Critical buckling load*

Initially, the finite element analysis is carried out to determine the critical buckling loads of the structures containing an embedded delamination. The eigenvalue analysis described in Section 2.1 is performed for models with various delamination lengths. For the flat panel model without delamination (i.e., $a/L = 0$), the critical buckling load is found to be $P_{cr} = 600$ kN. When the delamination exists within the panel, the buckling load decreases with increase in its length as shown in Fig. 3(a). However, this effect does not appear until the delamination length is nearly $a/L = 0.3$. The physical interpretation of this transitional delamination length is that the local buckling strength of small delaminated ligament section with the [0°] laminate (i.e., portion of the 4th layer with length $2a$) remains greater than that of the entire panel without any delamination. Thus the existence of a small delamination does not weaken the panel or lower P_{cr}. When the length becomes large

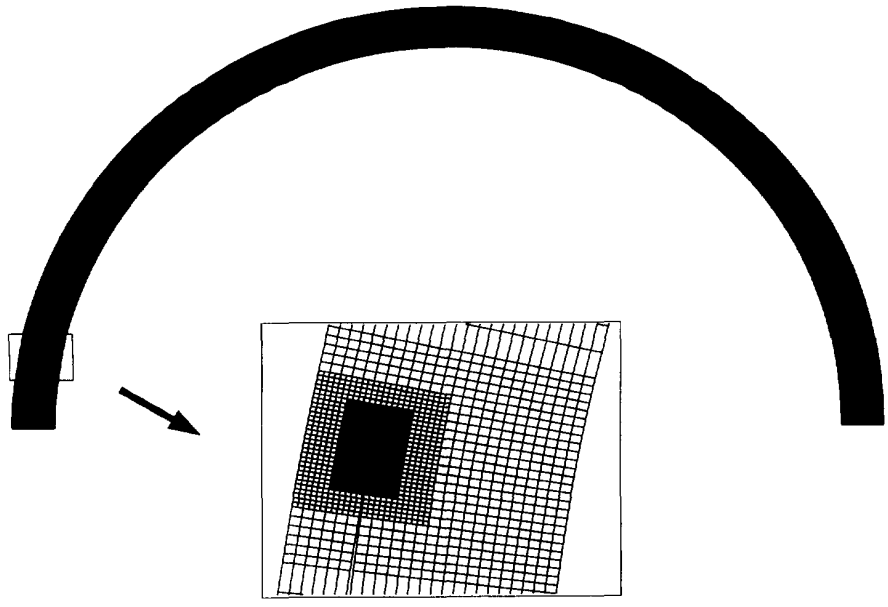

Fig. 2. Slightly deformed finite element mesh of the top half of cylindrical shell with the delamination angle $\theta = 10^\circ$. The near tip region is enlarged.

enough such that the local buckling load of the ligament section falls below 600 kN, the effective P_{cr} of the panel also decreases. Once the ligament section begins to buckle, it generates a bending moment around its roots (i.e., crack tip) and accelerates the buckling of the entire panel. This phenomenon may produce an unstable post-buckling behavior and will be discussed later.

As the ligament length increases beyond $a/L \simeq 0.6$, the ligament (4th layer) and the rest of the panel (1st to 3rd layers) deform more independently and the *rate* of decrease in P_{cr} slows down. Although not shown in the figure, the lowering of P_{cr} continues until $a/L = 0.9$ when $P_{cr} = 102$ kN. This value is equal to the sum of the buckling loads of two separate panels, one with $[0^\circ/90^\circ/90^\circ]$ and the other with $[0^\circ]$ laminae. Indeed at this delamination length, there is no coupling of the ligament and the rest of the panel, and they essentially buckle as independent structures. We note that the computed buckling mode of the flat panel with an embedded delamination exhibits overlapping of the ligament on the rest of the plate, which is physically inadmissible. In the pre- and post buckling analysis presented in the next section, a small delamination opening is prescribed in the initial geometry. This ensures the opening of the ligament during the loading.

The critical buckling load of the cylindrical shells containing delaminations of various lengths are shown in Fig. 3(b). The trend is similar to that observed in the flat panel model. When the crack arc length or the half delamination angle is $\theta \leqslant 5^\circ$, the critical pressure p_{cr} remains very close to that of the shell without a delamination (i.e., $\theta = 0^\circ$). As the delamination angle increases, the gradual loss of strength occurs. When $\theta \simeq 17^\circ$, the rate of decrease slows down and p_{cr} essentially levels off. Unlike the flat panel case, the relative extent of drop in the buckling pressure for long delamination is much smaller. For $\theta > 17^\circ$, the buckling mode shows a localized deformation of the delaminated region while the rest of the shell remains nearly circular. Such physical behavior may explain the stabilizing of p_{cr}. Also different from the flat panel results, the buckling modes of cylinders produce both opening and overlapping of delaminated region. Whether the delamination opens or overlaps depends on its location, laminate orientations and total number of laminae. These results and more precise description of the buckling mode shapes and how the perturbation is prescribed to the original geometries of the flat panel and cylindrical shell are summarized in Wu and Nakamura (1997). We note that, prior to reporting the results shown in Fig. 3, a rigorous mesh convergence study was performed. For the cylindrical shell with $\theta = 15^\circ$ shown in the figure has 8364 elements and $p_{cr} = 16.16$ MPa. With different mesh refinements,

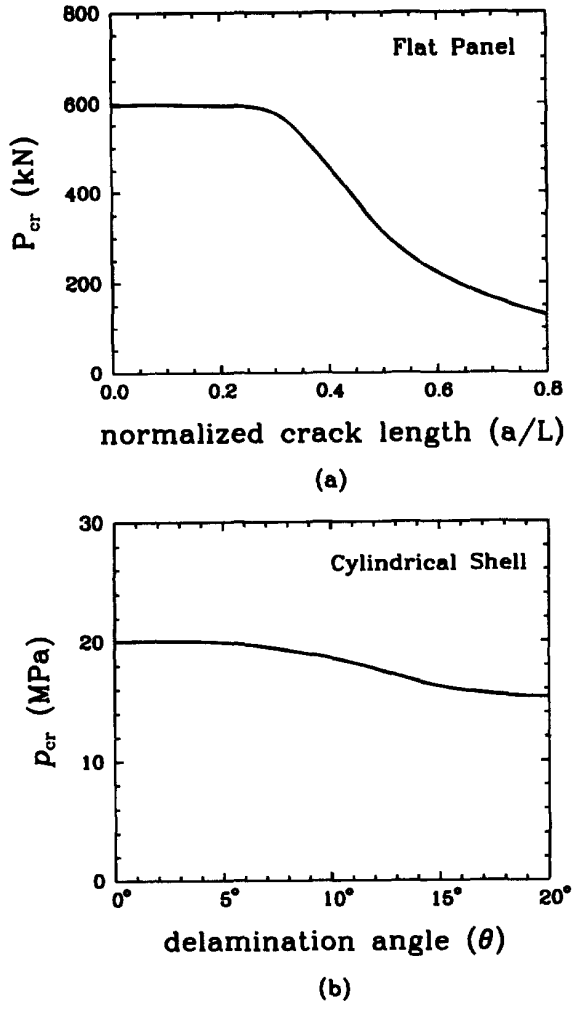

Fig. 3. Critical buckling load of composite structures containing different delamination sizes. (a) Critical axial load vs normalized delamination length. A large drop is observed when $a/L = 0.3$. (b) Critical external pressure vs the half delamination angle. A more gradual drop is observed.

the results are; $p_{cr} = 17.37$ MPa with 1116 elements, $p_{cr} = 16.72$ MPa with 3544 elements, and $p_{cr} = 16.14$ MPa with 13,001 elements.

4.2. *Pre- and post-buckling behavior of flat panel*

In order to determine the fracture parameters of the delamination and the deformation characteristics of the flat panel, we prescribed a small geometry perturbation (imperfection) in the shape of the critical buckling mode to the original mesh. This mesh is used in the pre- and post-buckling analysis. During the calculation, the displacement at the end-plane node is gradually increased over many increments and the reaction force is calculated as the equivalent axial load. In the quasi-static analysis, no delamination growth is simulated and the embedded delamination is assumed to remain stationary during loading. In Fig. 4, the progressive deformation of the panel, including the increasing opening of the delaminated ligament, during the post-buckling regime is shown for the model with $a/L = 0.4$. For each deformed state, the corresponding end-plane displacement and the axial load are noted. In this static analysis, no delamination growth is simulated, and the delamination length remains fixed in each model during loading. Prior to buckling, the amount of deformation is very small and the delamination essentially remains closed. The increasing end-point deflection associated with the decreasing load noted in the figure clearly indicates

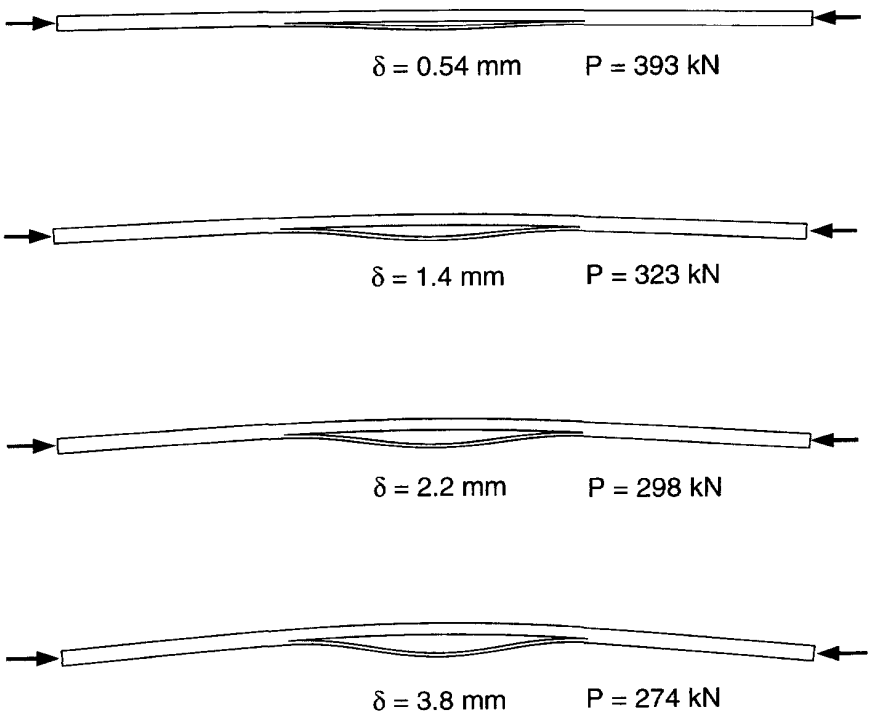

Fig. 4. Outlines of the flat panel with $a/L = 0.4$ at various stages of post-buckling deformation. Corresponding end-shortening displacement and axial load are noted.

the unstable buckling behavior of the panel. Also in the figure, two independent buckling modes, the ligament and the overall panel, can be observed.

The load versus deflection relationship of panels containing various delamination lengths are plotted in Fig. 5. For panels with a short delamination ($a/L \leqslant 0.2$), the crack never opens up (even with a substantial initial imperfection) and the panels behave identically to the one without any delamination. Although this post-buckling curve appears nearly horizontal, it has a small upward slope and the post-buckling behavior is characterized as *stable*. Once the delamination length reaches $a/L = 0.3$, the crack opens up and the initial post-buckling response exhibits highly *unstable* behavior. By carrying out

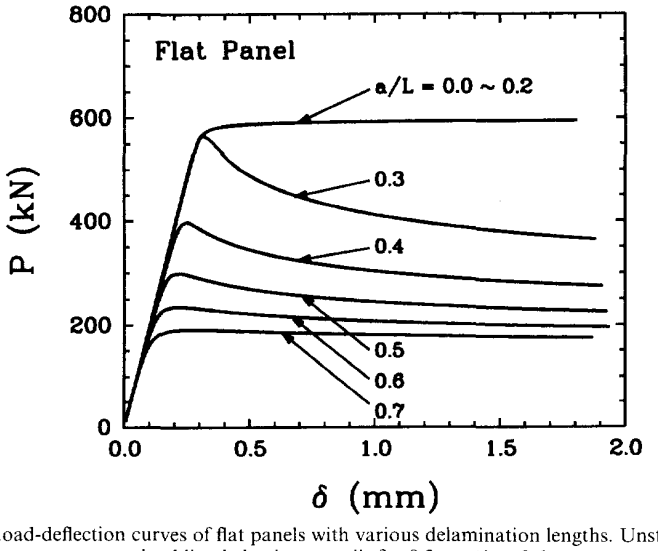

Fig. 5. The load-deflection curves of flat panels with various delamination lengths. Unstable initial post-buckling behavior prevails for $0.3 \leqslant a/L \leqslant 0.6$.

several calculations, we have determined the precise transitional delamination length (at which unstable post-buckling occurs) to be $a/L = 0.24$. The unstable post-buckling for panels with longer delamination is the result of the coupling of the two buckling modes, one by the ligament section and the other by the overall panel. When the ligament section begins to buckle, it creates a local root bending moment which promotes the buckling of the entire panel. This mechanism operates until $a/L \simeq 0.6$, and at this delamination length, the two sections begin to buckle independent of each other as described earlier. This explains the re-stabilizing of the post-buckling behavior for $a/L > 0.6$ shown in the figure. The maximum or peak load for each delamination length is nearly identical to the corresponding P_{cr} obtained by the eigenvalue analysis, shown in Fig. 3(a). This assures no excessive perturbation is added to the original geometry.

Except for the panels with very long delamination, the crack essentially remains closed prior to the buckling or during the pre-buckling stage. After the panel begins to buckle, the delamination opens and the energy release rate and the mixed-mode stress intensity factors are calculated using the domain integral forms given in (2) and (5). The results for energy release rate are plotted as a function of the end-shortening displacement δ in Fig. 6(a). The figure shows a rapid increase of $\mathcal{G}$ once the panel buckles, especially for the cases with shorter delamination length. As an example, a panel with $a/L = 0.3$ buckles at $\delta = 0.3$ mm and $\mathcal{G}$ increases rapidly for greater δ. In fact, it has its highest rate of increase during the

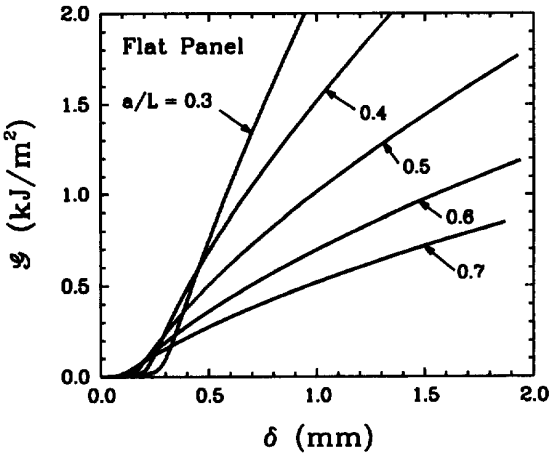

(a)

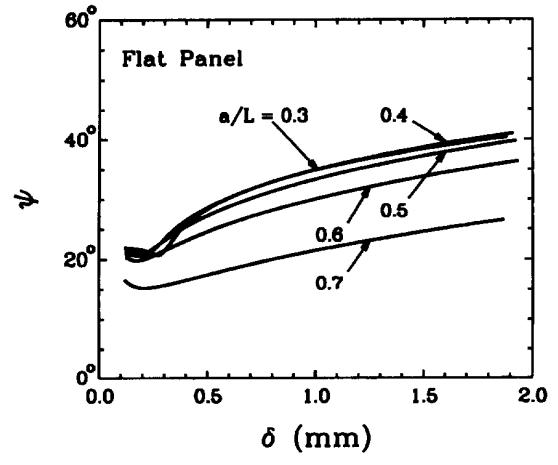

(b)

Fig. 6. (a) Energy release rate as a function of end-shortening displacement for flat panels with various delamination lengths. (b) Corresponding phase angle.

post-buckling stage. For the models with longer delaminations, the $\mathcal{G}$ increase is more gradual. The phase angle is also determined at every load increment from the computed mixed-mode stress intensity factors. In reporting the phase angle, the characteristic length is chosen to be $L = 100$ μm, which is a typical value used in many interface fracture analyses. The phase angle shown in Fig. 6(b) generally increases as the prescribed displacement increases. Note that the changes in ψ occur solely because of large displacement effects and not by a nonlinear material response. The panel is assumed to remain linear elastic throughout the calculation. In all cases, the increase in the phase angle implies a greater shear mode relative to the tensile mode in the near tip region.

4.3. *Pre- and post-buckling behavior of cylindrical shell*

The loading condition of the cylindrical model is imposed by the pressure applied on the outer most element layer of the shell. Throughout the calculation, the direction of the pressure at every element is always kept normal to its surface as it rotates during loading. Unlike the flat panel case, equivalent displacements can not be prescribed and the load increments are kept extremely small especially near the buckling load. The outline of the deformed cylindrical shell with the half delamination angle $\theta = 15^\circ$ at the pressure $p = 16.1$ MPa is shown in Fig. 7(a). The deformed geometry shows the bulging out of the outer delaminated ligament layer. This deformation shape is somewhat counter-intuitive since the ligament section bulges out against the large compressive pressure applied at the surface. To compare with the computationally simulated deformed shape, a post-test photograph of an actual specimen which underwent high pressure testing is shown in Fig. 7(b). Although many geometrical parameters including the total number and orientations of laminae are different and one must be careful in making any conclusions, both models clearly show the bulged out sections and the failure pattern of the specimen appears to be consistent with the deformed computational model. In the figure, the photograph represents the unloaded configuration of the specimen and shows a more circular shape (excluding the damaged region), while the deformed shape of the computational model shows a more elliptical shape due to its loaded state.

In order to measure the amount of deformation, we introduce a displacement parameter ω which defines the change in diameter of the shell along the symmetrical plane (see Fig. 8(b)). Under small external pressure, ω is linearly proportional to p, but as p approaches the buckling pressure, the increasing rate of ω changes. The results of ω as function of p for shells with different delamination angles ranging from $\theta = 0^\circ$ (no delamination) to 20°

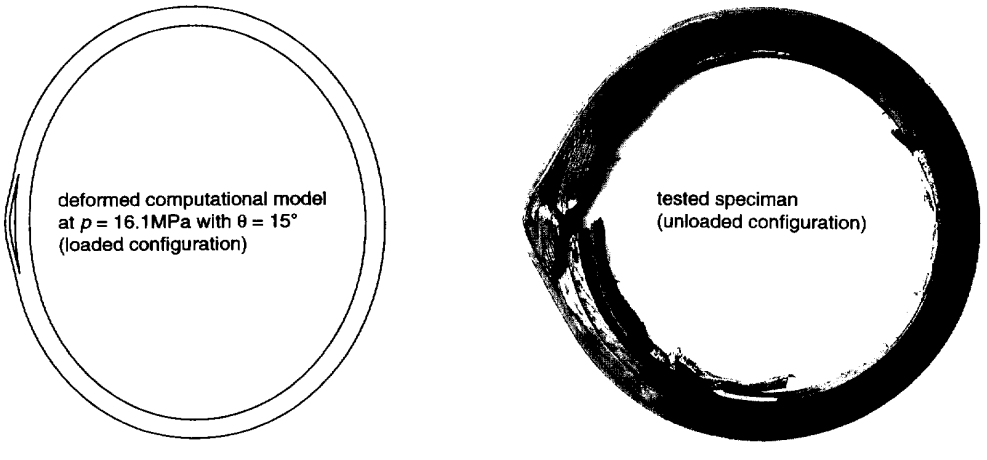

Fig. 7. (a) Deformed outline of the cylindrical shell containing an interlaminar delamination, showing the bulging out of the ligament. (b) Photograph by Hercules Aerospace Corp. which shows a cross-section of a composite cylinder which underwent high pressure testing. It also shows the damaged bulged-out section.

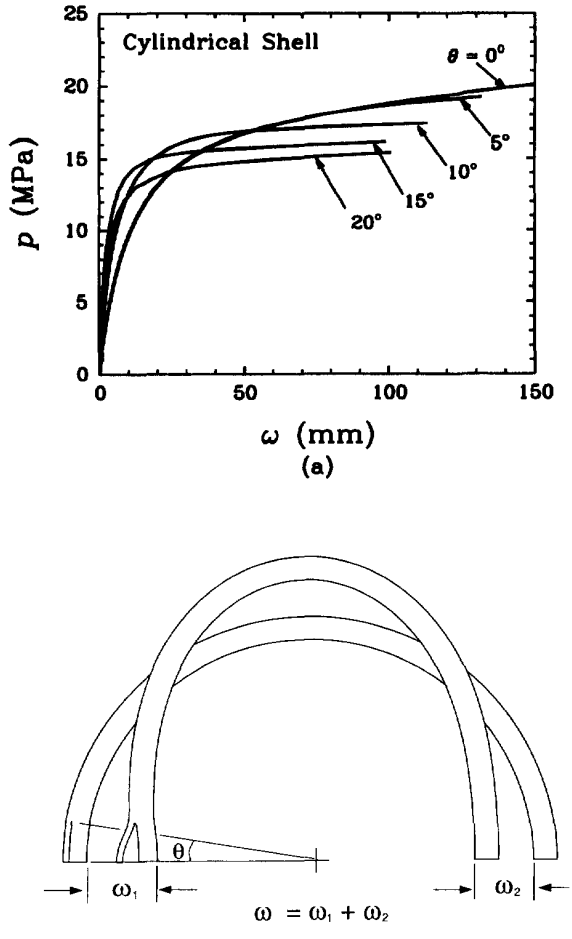

Fig. 8. (a) Pressure vs deformation parameter of cylindrical shells with various delamination angles. All results indicate stable post-buckling behavior. (b) Undeformed and deformed top-half of the shell, illustrating the definition of the deformation parameter ω.

are shown in Fig. 8(a). In Fig. 8(b), graphical representation of the displacement parameter ω is shown. Unlike the flat panel case, the cylindrical shell always exhibits increasing pressure with increasing deformation or stable post-buckling behavior regardless of the delamination size. However, the deformation increase with respect to pressure is slightly different in each case as described below.

Figure 8(a) exhibits the interesting characteristic that for small pressure levels, the apparent structural stiffness increases as the size of the delamination increases. The only exception to this is the twenty degree case which is initially softer than the fifteen degree case but stiffer than the ten degree case. As will be discussed later, the $\theta = 20^\circ$ case is not considered because it exhibits delamination ligament overlapping under all load levels. This apparently anomalous behavior is explained by the stress intensity factor histories shown in Fig. 9. As can be seen, K_I is initially negative for all delamination lengths. The interlaminar stress state associated with ligament bending imparts an outward rotation to the shell in the vicinity of the delamination. Figure 9(a) shows the slope of K_I vs p to change from negative to positive at 12 MPa. A further pressure increase causes the delamination to open up. This reversal in ligament bending is associated with a reversal in the sign of the incremental interlaminar bending moment at the delamination tip. Further pressure loading thus adds an incremental negative rotation to the shell in the vicinity of the delamination, shown in Fig. 8(a).

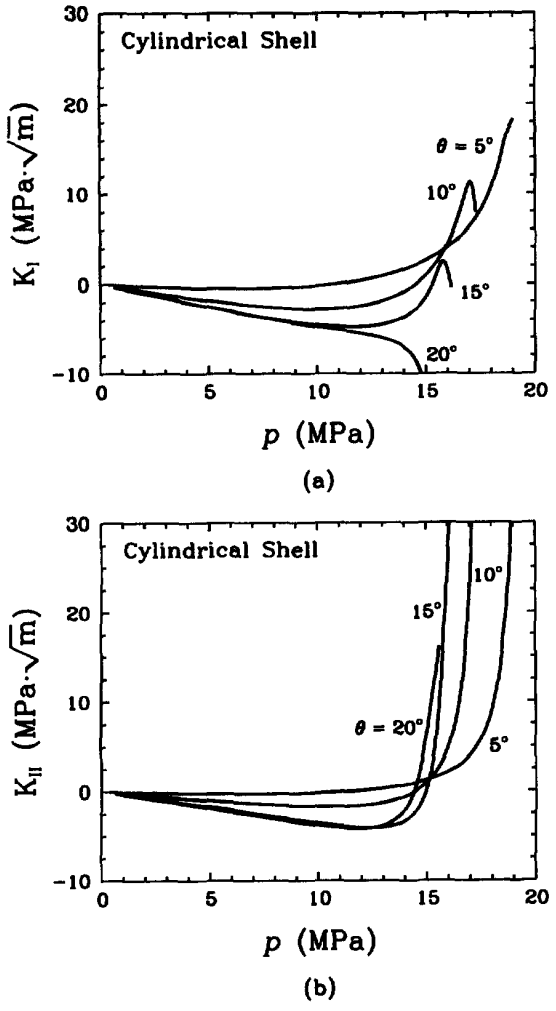

Fig. 9. Mixed-mode stress intensity factors for cylindrical shells with various delamination angles for (a) Mode I and (b) Mode II. Negative K_I corresponds to delamination in closure mode.

For a model with a larger delamination, the rapid increase of ω occurs more suddenly near its critical buckling pressure. In general, the deflection ω_2, opposite to the delamination, is slightly greater than ω_1 on the delamination side. The delamination side is locally stiffer due to its opening as shown in Fig. 8(b). In the cylindrical shell, a coupling of the ligament buckling and the buckling of the rest of the shell also occurs. Although more localized and with a smaller effect than the flat panel case, the bending moment generated by the ligament buckling pushes the other layers inward. This phenomenon explains the greater rate of increase in ω near the buckling load with a delamination. In addition, from the calculated reaction forces, we have found that the outer [0°] laminate carries up to 95% of the total circumferential load in the shell and the magnitude of the internal hoop stress is extremely high. The high compressive stress in this layer can trigger a kink band formation.

The evolution of the near tip state in the cylindrical model is more complex than that of the flat panel. First, the magnitude of compressive stress is at least several times greater than that of a flat panel at a same energy release rate. Second, the increase in the delamination opening displacement or the tensile mode is not always monotonic. The same is true for the shearing mode which switches its direction during the loading. In order to illustrate the evolution of the field surrounding the delamination, the mode I and II stress intensity factors are plotted in Fig. 9. For the mode I stress intensity factor shown in Fig. 9(a), all the models have negative K_I initially. This implies that the externally applied pressure closes

the delamination. However this does not always mean the crack faces overlap since the perturbation prescribed to the original geometry has a small initial crack opening. The magnitude of the crack closing displacement increases with the delamination size. In fact, for $\theta = 20^\circ$, the delamination never opens up and the crack faces eventually overlap at higher load. We have also carried out the calculations with contact elements but the results showed unstable computational behavior and are not presented here. For the cylindrical shells with shorter delamination, K_I becomes positive at higher pressure. However for $\theta = 10^\circ$ and 15°, the K_I increase is halted and it actually begins to decrease at some greater pressure. Somewhat similar results are seen for the mode II stress intensity factor in Fig. 9(b). In all cases, K_{II} is negative at lower pressure but changes its sign and increases rapidly at higher pressure. The abrupt decrease in K_I occurs at the same pressure level as the rapid increase in K_{II}. At this point the ligament opening is large and the delamination process is in transition from an opening to a peeling mode.

Although these events are worth noting, the evolution of the near tip field at low pressure has a small influence on the failure when it occurs at a much higher pressure. In order to investigate the crack driving force in the critical range, the energy release rate is plotted for the pressure range 13 MPa $< p <$ 16 MPa in Fig. 10(a). In the figure, the dashed-line portions for $\theta = 10^\circ$ and 15° indicate when K_I is negative and the delamination is in closure mode. Since the critical energy release rate of this laminate is assumed to lie in

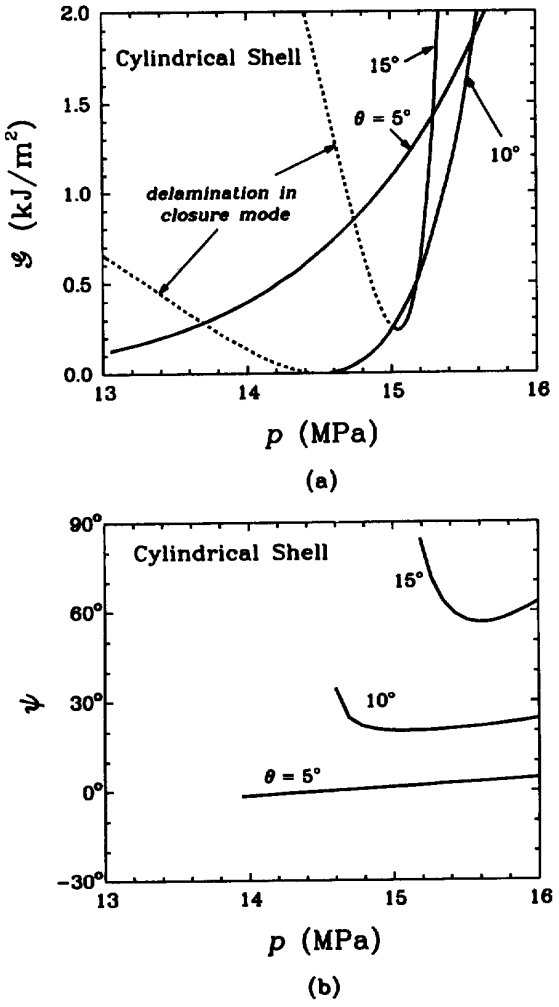

Fig. 10. (a) Energy release rate and (b) phase angle in the pressure range 13 MPa $\leqslant p \leqslant$ 16 MPa. The dashed lines indicate the delamination in closure mode ($K_I < 0$).

the interval $\mathcal{G}_c = 0.5$–1 kJ/m^2, the results predict delamination growth to occur when the pressure is $p = 15$–16 MPa, which is 75–80% of the buckling pressure of a flawless cylinder. This implies that failure by delamination growth can occur at a lower load than p_{cr} or prior to buckling. Delamination growth is thus predicted to be the critical failure mode in the pressurized shell. The phase angle at the same pressure range is also shown in Fig. 10(b). Unlike the flat panel case, a large variation in ψ is observed for different delamination angles. The model with $\theta = 5°$ has a tensile dominated field while a much greater shear mode is present in the model with $\theta = 15°$.

4.4. *Competition of failure modes—design diagram*

In a laminated structure containing an embedded flaw and subjected to large compressive load, possible failure modes can be characterized as structural buckling, delamination growth, kink band formation or any combination of them. Based on the results presented in the earlier sections and additional calculations, the primary failure mode for a particular structure and boundary condition is examined in this section. The main purpose is to identify a likely failure mode and use this information to strengthen the overall integrity of a structure. Obviously the determination of the primary failure mode or the initial source of failure depends on the shape of the model as well as its geometrical dimensions. For this analysis, we have selected the cylindrical shell as the model structure, and its shell thickness and radius are chosen as variable geometrical dimensions. For the flat panel model analyzed in the earlier sections, the dominant and important failure mode always appears to be buckling since the internal compressive stress never reaches the magnitude needed for the kink band formation, and the delamination growth is likely to occur only after buckling.

Initially the radius of the cylinder is set constant at $R = 0.2$ m while the shell thickness is varied. The initial embedded delamination size is assumed to be $\theta = 5°$. A smaller θ is not selected because such a delamination does not always open. In addition, we have found that a small variation in the delamination size does not affect the dominant failure mode. The location of the delamination and the stacking sequence of the laminae are assumed to be the same as those of the cylindrical model described earlier. In Fig. 11(a), the energy release rate of cylindrical shells with different thicknesses are shown. Although many different thicknesses are calculated, only the results of $t = 16$ mm, 20 mm and 24 mm are plotted for clarity. All three models have a similar rise of $\mathcal{G}$ except at the initial pressure when $\mathcal{G}$ starts to rise differently in each case. This initial critical pressure increases with the thickness of the model. Note the energy release rate does not scale with the thickness. In each model, the maximum compressive hoop stress σ_{hoop}^{max} is also recorded from the computed stress field within the entire shell during the loading. This information is needed in order to determine the critical pressure when the kink band formation is likely to occur in the fiber-reinforced laminae. The maximum compressive stress usually occurs in the outer most lamina adjacent to the delamination. As see in Fig. 11(b), this stress is not linearly proportional to the loading pressure at higher load level. At higher pressure loads, a large rotation apparently shifts the stress distribution within the shell and accelerates the rise of the stress.

Using these data for $\mathcal{G}$, σ_{hoop}^{max} and also the buckling pressure p_{cr} for models with different thicknesses, one can construct a diagram which contains three domains of failure mode. In order to specify the likely dominant failure mode, critical energy release rate $\mathcal{G}_c$ and the steady state kink band formation stress σ_{KB} of the laminate must be given. In constructing the diagram, we have fixed the critical energy release rate to be $\mathcal{G}_c = 0.72$ kJ/m^2. Although this particular value is chosen rather arbitrarily, it is in the range of several experimentally observed values of $\mathcal{G}_c$. Since $\mathcal{G}$ increases very rapidly once it starts to rise (see Fig. 11(a)), a variation of $\mathcal{G}_c$ within any reasonable range makes very small difference in the corresponding critical pressure for delamination growth. With these choices, the only remaining variables are the shell thickness t and the kink band stress σ_{KB}. Our aim is to draw lines which separate the domains of various dominant failure modes on the plane defined by t and σ_{KB}. Such a diagram is shown in Fig. 12(a), where the thickness is normalized by the shell radius. Here the transition boundary separates the domains of *delamination growth* and *kink band initiation*. In the figure, a vertical line is also drawn to separate the *buckling* domain. Our

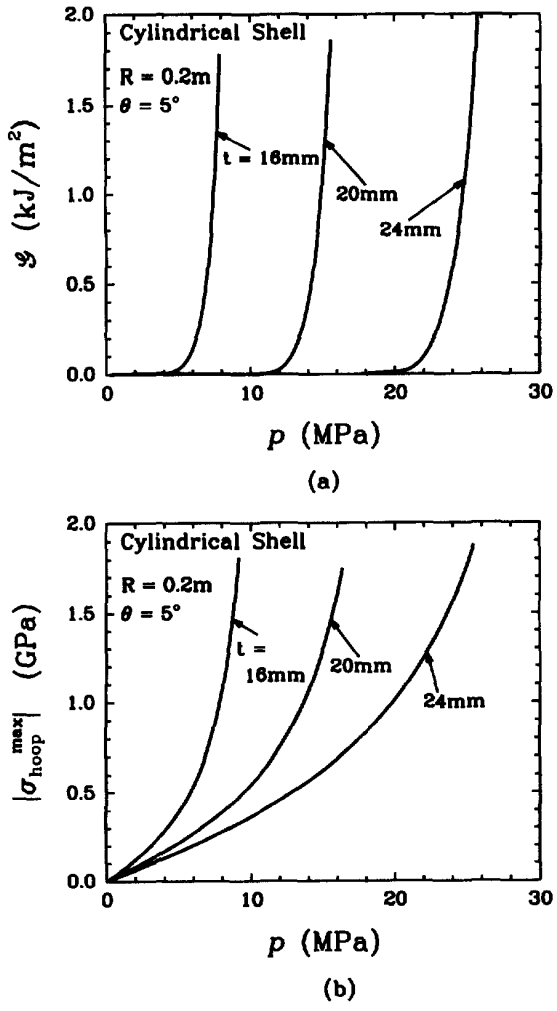

Fig. 11. (a) Energy release rate vs pressure for shells of different thickness. The radius is $R = 0.2$ m and the delamination angle is $\theta = 5°$. (b) Magnitude of the maximum hoop stress inside the shell. The magnitude increases with decreasing thickness.

computational results suggest that structural buckling occurs only after $\mathcal{G}$ reaches $\mathcal{G}_c$ and the magnitude of σ_{hoop}^{max} surpasses σ_{KB} regardless of the thickness. This means that buckling can not be predicted as the primary failure mode in any of the cylindrical shell geometries considered. However, very thin shells ($t/R \to 0$), which have small critical buckling pressure, may not have sufficient stiffness to sustain any sizable delamination growth or kink band expansion. Thus, in these shells, the structural buckling is more likely to take over as the dominant failure mode. Here, an operational condition for buckling is set for any shells whose buckling pressure is $p_{cr} < 1$ MPa. This happens when the normalized thickness is $t/R < 0.036$, and this domain is labeled as the buckling failure mode independent of σ_{KB} in the diagram. For thicker shells, one must first choose an appropriate kink band stress for a given fiber-reinforced composite material. For an example, if $\sigma_{KB} = 0.8$ GPa, then a horizontal line can be drawn at this stress level in the diagram, denoted as 'line A' in Fig. 12(a). Next, if the shell thickness is chosen as $t = 20$ mm, another line is drawn vertically at $t/R = 0.1$, denoted as 'line B' in the figure. The intersection of the two lines determines the failure mode of the given model. In this figure, it is marked as 'C' and falls within the kink band domain. Thus, this shell with specified properties and dimensions is more likely to fail by kink band formation. Such a process to find the failure mode may be useful in the design of shells since it identifies the weakest failure mode. In this example, one would know that increasing σ_{KB} directly benefits the overall integrity of the shell.

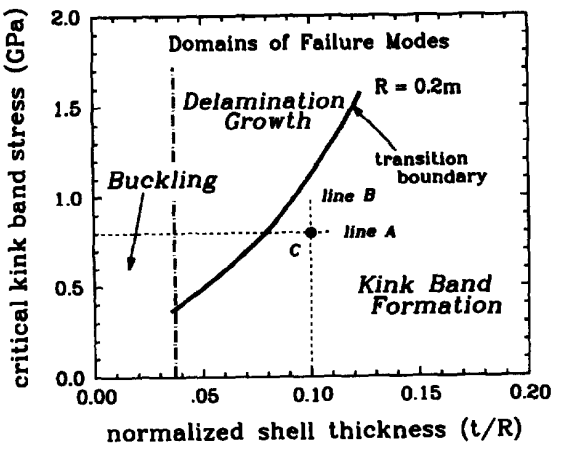

(a)

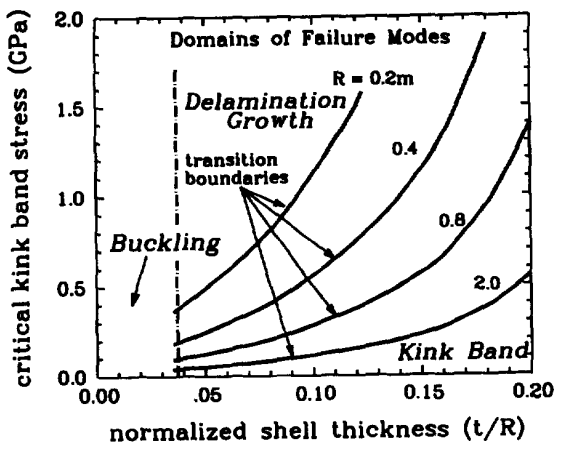

(b)

Fig. 12. Diagrams depicting domains of critical failure modes for a cylindrical shell with $\mathcal{G}_c = 0.72$ kJ/m^2. The delamination growth and kink band domains are separated by the transition boundary, while the buckling domain is shown for $t/R < 0.036$ which corresponds to $p_{cr} < 1$ MPa. The vertical axis represents the critical kink band formation stress for a given laminate. (a) For the shell with the radius $R = 0.2$ m. The point C is marked when $\sigma_{KB} = 0.8$ GPa and $t = 20$ mm are chosen. (b) For variable shell radius ranging from $R = 0.2$ m to 2 m. The transition boundary shifts downward as the radius increases.

In order to create a more comprehensive diagram, additional calculations are performed for shells with different radii. The results are shown in Fig. 12(b). The transition boundary which separates the delamination growth and the kink band formation shifts downward for shells with larger radius. Alternatively, as the radius increases, the domain of delamination growth enlarges and the likelihood of this failure mode increases. In fact, the diagram predicts that for a large shell with $R = 2$ m and $t < 400$ mm, the failure mode is always the delamination growth as long as $\sigma_{KB} > 0.6$ GPa, except possibly for very thin shells when the buckling mode can dominate. We caution, however, that these diagrams ignore many other factors which influence the failure characteristics of shells. The diagrams should be only used as approximate reference. Nevertheless, they still offer useful information in predicting a primary failure mode.

5. DYNAMIC ANALYSIS

The results for the flat panel presented in the earlier section suggest a possible unstable delamination growth in the post-buckling regime. Furthermore, laminated structures, both

flat panels and cylindrical shells, may react differently under dynamic loading condition due to inertial effects. In this section, we present behavior of these models under a rapidly increasing load. Dynamic delamination propagation is also simulated using a specified fracture criterion. As described in Section 2.3, there are not sufficient experimental data for the dynamic toughness of interfacial cracks in laminated structures. Here, we assume the growth initiation and the propagation of the delamination to be solely controlled by the energy release rate. More precisely, the required condition for delamination growth initiation is $\mathcal{G} = \mathcal{G}_d$ and a continuous growth is sustained if the condition $\mathcal{G} = \mathcal{G}_D$ is met. This assumption was also used in the simulation of interfacial crack propagations in a bimaterial specimen (Nakamura *et al.*, 1995) and the results agreed very well with the experimental record given by Lambros and Rosakis (1995). For the interface crack between graphite fiber-reinforced epoxy laminae modeled here, we have set the dynamic initiation toughness $\mathcal{G}_d$ as well as dynamic crack propagation toughness $\mathcal{G}_D$ to be $\mathcal{G}_d = \mathcal{G}_D = 0.72$ kJ/m^2 based on limited data available for this composite material. In general, the toughness or the resistance against fracture is influenced by the orientations of fibers, the loading rate, the phase angle and the crack tip velocity. If these factors were included, the near tip deformation and stress states at the initiation and propagation would certainly change. However, at the structural level, the present criterion, i.e., fixed toughness condition, should still yield an accurate description of the deformation behavior. During the propagation simulation, a correct crack tip velocity must be found so that the crack driving force or the available $\mathcal{G}$ is always equal to $\mathcal{G}_D$. In the finite element analysis, such a condition is only achieved accurately through an iterative process. An effective computational procedure for the dynamic crack propagation which incorporates this process was developed by Lo *et al.* (1994) and is employed here.

5.1. *Flat panel model*

In the dynamic analysis of the flat panel, an initial delamination length is assumed to be $a_o/L = 0.3$ and the subsequent delamination propagation from this length is simulated. The location of the initial embedded delamination and the orientations of laminae are identical to the model shown in the static analysis. Equal dynamic loads are applied simultaneously at both ends of the panel so that the symmetry condition is still preserved across the middle vertical plane. A similar mesh for the half-model is also used but the region of near tip elements is extended to accommodate the growing delamination tip. Unlike the static case where the loading is controlled by the prescribed end displacement, it is applied as a uniform pressure on the element faces across the end plane in the dynamic analysis. Initially, the magnitude of pressure is linearly increased with time and the rate of resultant force is set as $\dot{P} = 25$ MN/s. For $t > 40$ ms or after P reaches 1 MN, the magnitude of the load is held constant with respect to time. These rate and magnitude are chosen after a few trial calculations so that the buckling occurs while the structural inertia is still important and the delamination grows at sufficiently high speed. The delamination path is assumed to remain on the interlaminar boundary and no kinking out of the interface is modeled. The computations are carried out for about 32 ms after the initial load is applied and terminated when the crack tip propagates outside the region of near tip fine elements.

The dynamic energy release rate is calculated using (2) and the results are shown in Fig. 13(a). It takes about 15 ms for sufficient load to build up and the delamination begins to open up. The energy release rate shows a gradual increase as the structure enters the post-buckling regime at this elapsed time. At around $t = 30$ ms, $\mathcal{G}$ shoots up, indicating a sudden increase of the deformation associated with the buckling. When $\mathcal{G}$ reaches the critical initiation toughness, $\mathcal{G}_d = 0.72$ kJ/m^2 at $t = 31.4$ ms, the displacement constraint holding the crack tip node is released and propagation begins. During the delamination propagation, the dynamic $\mathcal{G}$ is always maintained at $\mathcal{G}_D = 0.72$ kJ/m^2 to satisfy the propagation criterion. To control the dynamic $\mathcal{G}$ at this level, a suitable crack tip velocity at every increment is found using the iterative technique. The resulting velocity as it accelerates after the initial growth is shown in Fig. 13(b). In the finite element model, the delamination is simulated to propagate over 21 elements or $\Delta a = 4.5$ mm over the time period of about

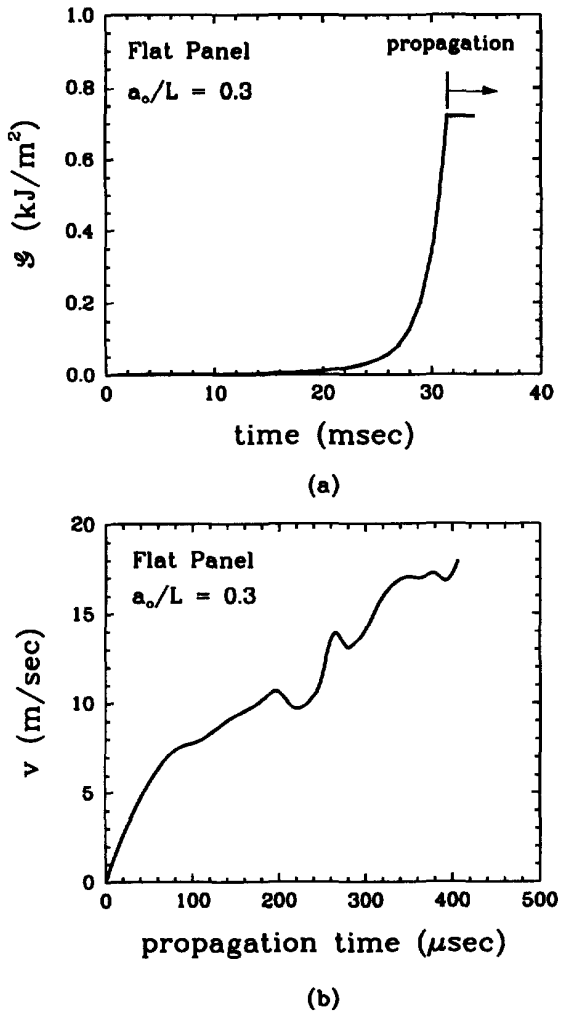

Fig. 13. (a) Dynamic energy release rate for the flat panel during stationary and propagation phases. The delamination starts to grow when $\mathcal{G}$ reaches $\mathcal{G}_d = 0.72$ kJ/m^2 at $t = 31.4$ ms. (b) The resulting crack tip velocity during propagation phase.

400 μs. At the last calculated increment, the velocity is about 18 m/s. If the similar increase in v continues for greater t, the whole panel should separate within about 5 ms.

5.2. *Cylindrical shell model*

A similar analysis is also carried out for the cylindrical shell model. Here, the initial half delamination angle is assumed to be $\theta_o = 5^\circ$ and a linearly increasing pressure with respect to time is applied at the outer shell. The loading rate is set at $\dot{p} = 3.2$ GPa/s. The results of dynamic $\mathcal{G}$ after the load application are shown in Fig. 14(a). For this model, the energy release rate begins to increase at a much earlier time than the flat panel result. Although the two models have comparable dimensions, the difference is quite significant. One reason is that the location of the delamination is much closer to the load application boundary in the cylindrical case. A more important reason is that for the flat panel, the delamination opening requires buckling of the panel while that of the cylindrical model occurs prior to the buckling. Therefore, a much earlier rise in $\mathcal{G}$ is possible in the cylindrical shells. The figure also shows an oscillatory behavior for $t < 3.8$ ms. This can be attributed to the inertial effect due to the pressure wave from the outer layer since it initially pushes the delaminated ligament inward. Indeed, the computed dynamic K_I is negative during this period. Although such a closure mode is not physically possible, the calculations still show

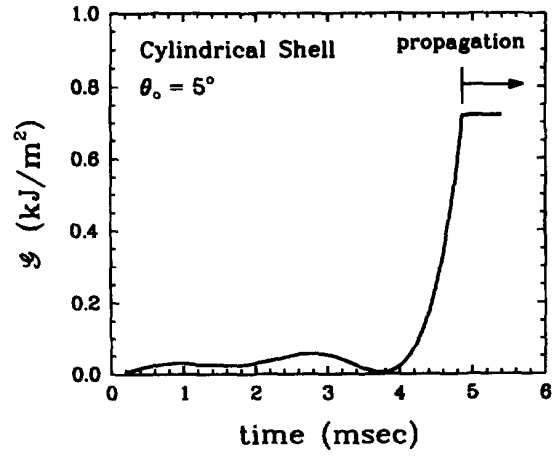

Fig. 14. (a) Dynamic energy release rate for cylindrical shell during the stationary and propagation phases. The delamination starts to grow when $\mathcal{G}$ attains $\mathcal{G}_d = 0.72$ kJ/m^2 at $t = 4.86$ ms. (b) The resulting crack tip velocity during propagation phase.

finite $\mathcal{G}$. However, since the magnitude of $\mathcal{G}$ at the initial phase is only a small fraction of $\mathcal{G}_d$, this process should not affect the deformation state of the shell at the subsequent delamination growth. At later time, the ligament starts to bulge out (similar to the statically deformed shell shown in Fig. 7(a)), and $\mathcal{G}$ begins to increase monotonically. At $t = 4.86$ ms, it reaches $\mathcal{G}_d$ and the propagation begins. The dynamic propagation is simulated over $\Delta a = 5$ mm or 22 element lengths during the total propagation time period of 50 μs. At the end of simulation, the crack tip velocity reaches $v = 170$ m/s, as shown in Fig. 14(b). This value is a significant fraction of material wave speed and almost an order of magnitude larger than that of the flat panel. The faster delamination speed may be attributed to greater stored energy available to drive the propagation. The cylindrical shell has much higher internal stresses than those of the flat panel for a given energy release rate. If the increase in v continues at a similar rate, complete failure of the shell is predicted within a sub-millisecond time period.

In order to illustrate the dynamic deformation of the shell at the structural level, the deformation parameter ω (shell narrowing along the symmetry line) is plotted in Fig. 15(a). The figure shows a smooth increase of ω with respect to time. The deformation parameter is also shown with respect to the pressure applied at the outer boundary in Fig. 15(b). Note the pressure increase is linearly proportional to time. The dynamic result is compared with

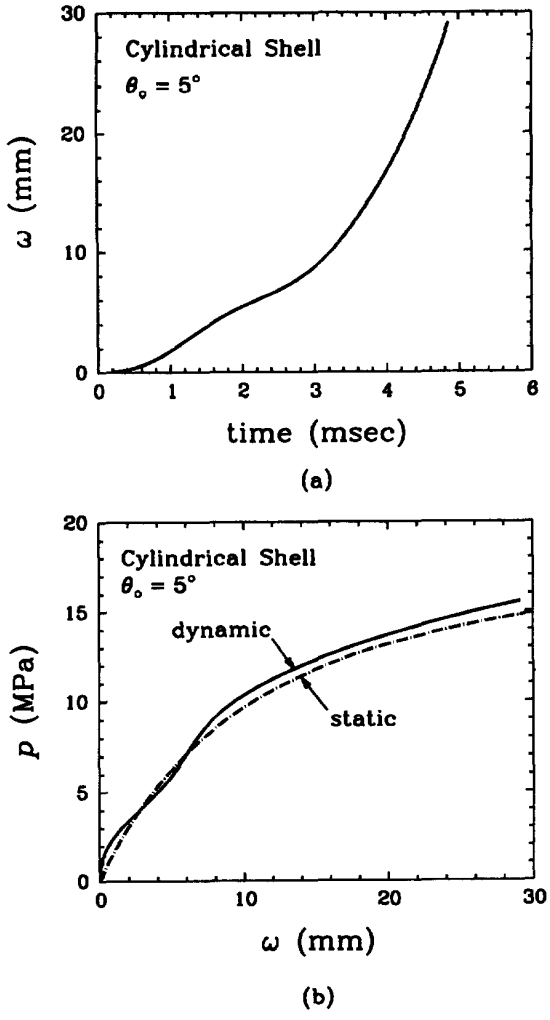

Fig. 15. (a) The deformation parameter ω under dynamic loading condition shown as a function of time. (b) The deformation parameter and corresponding pressure under dynamic and static loading conditions.

the corresponding static result in the figure. The two cases are in a good agreement, but with the dynamic case generally having smaller deformation than that of the static case. Such a result is expected since some inertia induced response time lag should exist for the dynamic case. The load is applied at the outer surface while ω is measured at the inner shell. However near $p \simeq 5$ MPa, a greater ω is observed for the dynamic case. It is probably due to the initial inertial effect by the stress wave, which is consistent with the oscillatory $\mathcal{G}$ observed at $t = 1 \sim 3$ ms. The energy release rate is also shown for the dynamic and static cases as functions of applied pressure in Fig. 16. The results show a greater difference in the two cases. The dynamic $\mathcal{G}$ trails the static $\mathcal{G}$ by the pressure level of about 1 MPa. In fact at the critical value of $\mathcal{G} = 0.72$ kJ/m^2, the corresponding pressures are 15.55 MPa and 14.58 MPa for the dynamic and static cases, respectively. This suggests, for the cylindrical shell, that the static relationship for $\mathcal{G}$ and p is more conservative than the dynamic relationship if similar critical fracture toughnesses are assumed for the static and dynamic cases. If a larger toughness prevails under the dynamic loading (as in many materials), then the difference in the critical pressures leading to delamination growth is even greater. In the figure, the dynamic $\mathcal{G}$ rises only up to 0.72 kJ/m^2 because the delamination growth condition is imposed to simulate the propagation for this case.

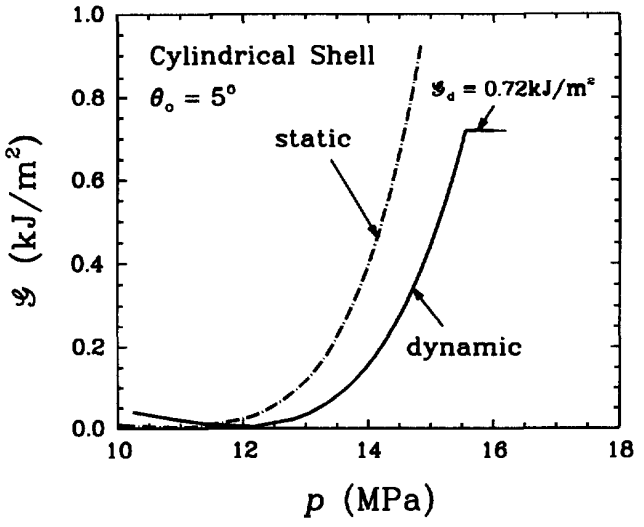

Fig. 16. The energy release rate shown as a function of the applied pressure for the dynamic and static cases. The results are shown for large pressure, $p \geq 10$ MPa. Note the dynamic $\mathcal{G}$ levels off at 0.72 kJ/m^2 since the toughness criterion is imposed during propagation. The static $\mathcal{G}$ continues to increase since no condition is applied.

6. DISCUSSION

A comprehensive analysis is carried out for different laminated structures subjected to a compressive load. In particular, two types of structures containing an interlaminar delamination are considered and their deformation characteristics are carefully analyzed with a view toward identifying dominant failure mechanisms. Some important structural deformation modes are observed in the flat panel model. When the panel contains an embedded delamination and is under uniaxial compressive load, a coupling of the global panel buckling and the local ligament buckling produces "unstable" post-buckling behavior. Such a condition is potentially hazardous for the integrity of structures. The energy release rate of the embedded delamination also increases rapidly during the unstable post-buckling phase. The rapid increase in energy release rate may cause delamination growth which may further reduce the compressive strength. The large shear stress observed during the loading may play an important part in defining composite material level failure. Fibers are very stiff under axial or transverse loading but are compliant under incremental shearing because of the low plastic shearing resistance of matrix. Therefore, embedded delamination will accelerate the development of kink bands and other local failure conditions.

A similar analysis is carried out for a composite cylindrical shell. The results show that a delamination reduces the critical buckling load but the structure still preserves its stable post-buckling behavior. The important difference observed in the cylindrical shell is that the energy release rate of the interlaminar delamination increases prior to the structural buckling. This lowers the critical structural failure load of shells and makes delamination growth a more critical failure mode. It was observed that initial crack closure prior to ligament buckling caused an apparent stiffening of the shell. Using an approximate $\mathcal{G}_c$ as a reference, the critical pressure for delamination growth is found to be about 80% of the buckling load. In addition, the internal compressive stress is much higher in the cylindrical shell than in the flat panel. Such a result increases the likelihood of compressive kink band formation in the laminate.

Based on various calculations, we have introduced a "design diagram" which identifies the dominant failure mechanism for the cylindrical shell. Three failure modes, structural buckling, delamination growth and kink band formation are assumed as possible mechanisms. With given geometrical dimensions and material properties, one can use the diagram to predict the primary failure mode or the initial source of failure. In general, the possibility

of delamination growth increases with shell radius while structural buckling is predicted for thinner shells. This diagram can be used effectively in designing shells with optimized shell radius and thickness for given toughness of interlaminar delamination and kink band formation stress.

Finally, we have simulated the dynamic crack propagation of interlaminar delaminations. Lacking any experimental data, we employed a simplified toughness condition and an iterative method to propagate the crack without prior input of the crack tip velocity history. The analysis of the two models under dynamic loading conditions shows that a much higher crack tip velocity is predicted for the cylindrical shell. The faster velocity in the cylindrical model is probably the result of greater stored energy available for delamination propagation. The cylindrical shell has greater stored energy than the flat panel when delamination growth initiates, as represented by the very large internal compressive stress in the laminae. The comparison of the static and the dynamic results for the cylinder has shown that the equivalent static pressure overestimates the energy release rate in the dynamic loading. Combined with expected higher toughness, delamination growth under dynamic conditions most likely occurs at a much larger pressure level than that of the static case.

Acknowledgements—The authors gratefully acknowledge the support of ONR under Grant # N0001491J1352. The photograph of the composite specimen tested by Hercules Aerospace Corp. shown in Fig. 7(b) was provided by the Carderock Division of the Naval Surface Warfare Center. Computations were performed on DEC AXP3000. The finite element analysis was carried out with the ABAQUS code, which was made available under academic license from Hibbitt, Karlson and Sorenson, Inc. Providence RI.

REFERENCES

Bijlaard, P. P. and Fisher, G. P. (1962) Column strength of H-sections and square tubes in post-buckling range of component plates. *NACA TN* 2994.

Chai, H., Babcock, C. D. and Knauss, W. G. (1981) One dimensional modeling of fracture in laminated plates by delamination buckling. *International Journal of Solids and Structures* **17,** 1069–1083.

Fleck, N. A., Deng, L. and Budiansky, B. (1995) Prediction of kink width in compressed fiber composites. *Journal of Applied Mechanics* **62,** 329–337.

Grady, J. E. and Sun, C. T. (1986) Dynamic delamination crack propagation in graphite/epoxy laminate. In *Composite Materials: Fatigue and Fracture*, ASTM STP 907, ed. H. T.. Hahn. American Society for Testing and Materials, Philadelphia, pp. 5–31.

Horban, B. and Palazotto, A. (1987) Experimental buckling of cylindrical composite panel with eccentrically located circular delaminations. *Journal of Spacecraft and Rockets* **24,** 349–352.

Jelf, P. M. and Fleck, N. A. (1992) Compression failure mechanisms in unidirectional composites. *Journal of Composite Materials* **26,** 2706–2721.

Jones, R., Broughton, W., Mousley, R. F. and Potter, R. T. (1985) Compression failures of damaged graphite epoxy laminates. *Composite Structures* **3,** 167–186.

Kardomateas, G. A. and Schmueser, D. W. (1988) Buckling and post-buckling of delaminated composites under compressive loads including transverse shear effects. *AIAA Journal* **26,** 337–343.

Lambros, J. and Rosakis, A. J. (1995) Dynamic decohesion of bimaterials: experimental observations and failure criteria. *International Journal of Solids and Structures* **32,** 2677–2702.

Liu, X. H. and Shih, C. F. (1995) A micromechanics model for incipient compressive kinking in fiber composites. Brown University Report.

Lo, C. Y., Nakamura, T. and Kushner, A. (1994) Computational analysis of dynamic crack propagation along a bimaterial interface. *International Journal of Solids and Structures* **31,** 145–168.

Moran, P. M., Liu, X. H. and Shih, C. F. (1995) Kink band formation and band broadening in fiber composites under compressive loading. *Acta Metallica et Materiala* **43,** 2943–2958.

Nakamura, T., Kushner, A. and Lo, C. Y. (1995) Interlaminar dynamic crack propagation. *International Journal of Solids and Structures* **32,** 2657–2675.

Qu, J. and Bassani, J. L. (1989) Cracks on bimaterial and bicrystal interfaces. *Journal of the Mechanics and Physics of Solids* **37,** 417–433.

Sheinman, I. and Soffer, M. (1991) Post-buckling analysis of composite delaminated beams. *International Journal of Solids and Structures* **27,** 639–646.

Shivakumar, K. N. and Whitcomb, J. D. (1985) Buckling of a sublaminate in a quasi-isotropic composite laminate. *Journal of Composite Materials* **19,** 2–18.

Simitses, G. J., Sallam, S. and Yin, W. L. (1985) Effect of delamination of axially loaded homogeneous laminated plates. *AIAA Journal* **23,** 1437–1444.

Stroh, A. N. (1962) Steady state problems in anisotropic elasticity. *Journal of Mathematical Physics* **41,** 77–103.

Sun, C. T. and Manoharan, M. G. (1989) Growth of delamination cracks due to bending in a $[90_5/0_5/90_5]$ laminate. *Composites Science Technology* **34,** 365 377.

Suo, Z. (1990) Singularities, interfaces and cracks in dissimilar anisotropic media. *Proceeds of the Royal Society of London* **A427,** 331–358.

Ting, T. C. (1986) Explicit solution and invariance of the singularities at an interface crack in anisotropic composites. *International Journal of Solids and Structures* **22,** 965–983.

Tvergaard, V. (1976) Buckling behavior of plate and shell structures. In *Theoretical Applied Mechanics*, ed. Koiter, W. T. North-Holland Publishing Co., The Netherlands, pp. 233–247.

Van der Neut, A. (1969) The interaction of local buckling and column failure of thin-walled compression members. In *Proceedings of the 12th International Congress of Applied Mechanics*, ed. Hetenyi, M. and Vincenti, W. G. Springer, Berlin, pp. 389–399.

Wang, S. S. (1984) Edge delamination in angle-ply composite laminates. *AIAA Journal* **22,** 256–264.

Wang, S. S., Suemasu, H. and Zahlan, N. M. (1984) Interlaminar fracture of random short-fiber SMC composite. *Journal of Composite Materials* **18,** 574–594.

Wang, S. S., Zahlan, N. M. and Suemasu, H. (1985) Compressive stability of delaminated random short-fiber composites, part I—modeling and method of analysis, part II—experimental and analytical results. *Journal of Composite Materials* **19,** 296–333.

Wu, L. C. and Nakamura, T. (1997) Effect of stacking sequence in composite laminates containing embedded delamination. (In preparation).

Yang, W., Suo, Z. and Shih, C. F. (1991) Mechanics of dynamic debonding. *Proceedings of the Royal Society of London* **A433,** 679–697.

Yin, W. L. (1988) The effects of laminated structure on delamination buckling and growth. *Journal of Composite Materials* **22,** 502–517.